Phosphorene–Fullerene nanostructures: A first-principles study

Diego Cortés-Arriagada[1,*], *Daniela E. Ortega*[2]

[1]Programa Institucional de Fomento a la Investigación, Desarrollo e Innovación. Universidad Tecnológica Metropolitana. Ignacio Valdivieso, 2409, San Joaquín, Santiago, Chile. *E-mail address: dcortes@utem.cl

[2]Centro Integrativo de Biología y Química Aplicada (CIBQA), Universidad Bernardo O'Higgins, General Gana 1702, Santiago, 8370854, Chile

Abstract. Hybrid materials formed by carbon fullerenes and layered materials have emerged due to their advantages for several technological applications, and phosphorene arises as a promising two-dimensional semiconductor for C_{60} adsorption. However, the properties of phosphorene-fullerene hybrids remain mainly unexplored. In this work, we employed density functional theory to obtain structures, adsorption energies, electronic/optical properties, binding (AIM, NBO), and energy decomposition analyses (ALMO-EDA) of nanostructures formed by phosphorene and fullerenes (C_{24} to C_{70}). We find fullerenes form covalent and non-covalent complexes with phosphorene depending on the molecular size, showing remarkable stability even in solution. Two classes of covalent complexes arise by cycloaddition-like reactions: the first class, where short-range effects (charge-transfer and polarization) determines the stability; and the second one, where short-range effects decay to avoid steric repulsion, and balanced long-range forces (electrostatics and dispersion) favors the stability. Otherwise, high-size fullerenes (C_{50} to C_{70}) only form non-covalent complexes due to strong repulsion at shorter intermolecular distances and lack of dissociation barriers. In terms of electronic properties, fullerenes act as mild *p*-dopants for phosphorene, increasing its polar character and ability to acquire induced dipole moments (polarizability). Also, small energy-bandgap fullerenes (<0.8 eV) largely increase the phosphorene metallic character. We also note fullerenes retain their donor/acceptor properties upon adsorption, acting as active sites for orbital-controlled interactions and maximizing the phosphorene light absorbance at the UV-Vis region. Finally, we strongly believe our study will inspire future experimental/theoretical studies focused on phosphorene-fullerene uses for storage, anode materials, sensing, phosphorene bandgap engineering, and optoelectronics.

Keywords: Phosphorene; DFT calculations; nanotechnology; composites; nanostructures; surface science.

1. Introduction

Among low-dimensional carbon allotropes (such as graphene and carbon nanotubes), the buckminsterfullerene molecule (C_{60}) is a class of 0-dimensional (0-D) organic compounds of spherical molecular shape and high surface area, displaying remarkable physical and chemical properties due to surface/interfacial effects and quantum confinement[1]. In particular, C_{60} displays a remarkable electron acceptor character with a semiconductor bandgap. Also, C_{60} is merely composed of sp^2-hybridized carbon atoms, which confer it an electron-deficient polyalkene nature, and thus, it is chemically reactive[1]. Likewise, small fullerenes have been synthesized and characterized (e.g., from high-resolution transmission electron microscopy), which have associated an increased reactivity with attaching to substrates because of containing paired or adjacent pentagons[2-3], and their electronic properties are significantly influenced by the shape and size [4]. The unique properties of fullerenes turn into useful building blocks for constructing supramolecular assemblies and micro/nanofunctional materials[1]. Consequently, non-covalent and covalent nanostructures have been fulfilled by depositing fullerene onto emerging low dimensional substrates such as graphene, perovskites, graphite-like carbon nitride, transition-metal disulfides, and hexagonal boron nitride[1, 5]. These hybrid nanostructures show potential applications in different technologies such as catalysis, nanoelectronics, optoelectronics, storage, batteries, solar cells, and spintronics, among others[1, 5].

Phosphorene emerged as a new generation of nanomaterials with an anisotropic 2-dimensional (2-D) structure in a puckered honeycomb shape with sp^3-orbital hybridization[6]. Relevant properties of phosphorene are high electrical conductivity ($2 \cdot 10^5$ cm^2 V^{-1} s^{-1}), high carrier mobility (≈1000 cm^2 V^{-1} s^{-1}), high thermal conductivity (4840–5300 W m^{-1} K^{-1}), and high tensile strength up to 130 GPa[6-8]. Phosphorene also displays a remarkable ability to bind

organic/inorganic molecules through covalent or non-covalent interactions, mainly favored by electrostatic attraction[9-12]; thus, phosphorene emerges as an ideal template for the formation of well-ordered structures for assembly of fullerenes and related phosphorene/organic nanostructures. Furthermore, surface coordination of phosphorene has been shown to enhance its stability under air/water dispersion, which is a major challenge in practical applications[13-15]. Despite widespread works on hybrids of fullerenes with other 2D nanomaterials, studies on Phosphorene-Fullerene hybrids have infrequently been reported and mainly focused on C_{60} adsorption. Experimentalists and theoreticians have synthesized/proposed Phosphorene–C_{60} nanostructures with relevant properties for technological applications such as high specific capacity battery electrode materials[16], solar energy conversion[17-18], new molecular doped crystalline superlattices for semiconductor industry[19], and heterojunction photodetectors[20]. In this way, properties of phosphorene and fullerenes are compensated synergistically; for example, it is found in photovoltaic research that fullerenes act as excellent electron acceptors in polymer solar cells, while phosphorene improves the energy alignment in the devices, which lead to improved power conversion efficiency by favoring the charge transfer and exciton dissociation[18].

Additionally, the packing of fullerenes onto substrates must be influenced by the shape and size, which would play a key role in the properties and stability of Phosphorene–Fullerene hybrids; then the physical/chemical phenomena that dominate the interaction strength is essential to be clarified. Mechanochemical reactions in a high energy mechanical milling process have been used as a strategy to form phosphorus-carbon (P−C) bonds between phosphorene and carbon materials, including C_{60}, graphite, and graphite oxide[16]; in this way, the content of the P−C bond in the phosphorene-C_{60} hybrids is only 0.8%, denoting C_{60} is not preferably bonded to phosphorene *via* covalent interactions until breaking the sp^2 C=C/C−C bonds to form defects[16]. In addition, low-

temperature scanning tunneling microscopy, X-ray, ultraviolet photoelectron, and scanning tunneling spectroscopy measurements also show that C_{60} molecules are mainly physisorbed at room temperature on the honeycomb lattice of blue and black phosphorene synthesized by epitaxial growth, where an interfacial charge transfer is evidenced upon interaction with C_{60}[21-22]. The Phosphorene-C_{60} non-covalent interaction has also been confirmed by the disappearance of the C_{60} absorption band at 340 nm in phosphorene Langmuir–Blodgett films after a simple toluene wash[20]. In this regard, density functional theory (DFT) computations supported a simple physical interaction between C_{60} and phosphorene characterized by strong electron density rearrangements (charge transfer) and adsorption energies of ~1 eV[22-23].

The background mentioned above indicates phosphorene could be implemented as a remarkable substrate for the assembly of novel hybrid nanostructures with carbon fullerenes. Nevertheless, it is still not well understood yet the influence of fullerenes size on Phosphorene-Fullerene hybrids' properties, such as the stability and preferred binding mechanism (covalent/non-covalent), electronic/optical properties after bonding, and the contribution of intermolecular forces determining the adsorption stability. To answer these questions, we employed a dispersion-corrected DFT scheme to obtain adsorption energies and conformations, electronic/optical properties, electron density-based analyses, and energy decomposition analyses of Phosphorene–Fullerene nanostructures, which provide deep insights into the stability, structure, adsorption mechanism, and useful potential properties for technological applications. We consider either the covalent or non-covalent binding of fullerenes in different sizes and symmetries as representative classes, i.e., C_{24} (D_{6h}), C_{26} (D_{3h}), C_{34} (C_2), C_{36} (D_{2h}), C_{40} (D_2), C_{44} (D_2), C_{50} (D_3), C_{60} (I_h), and C_{70} (D_{5h}); in this way, it is provided a wide family of adsorbates resulting in different assemblies for characterization.

2. Computational Details

We used the PBE functional with the all-electron def2-SVP basis sets for all the DFT calculations in the ORCA4.1[24-26]. The PBE functional has been used to describe the interactions of phosphorene with a wide range of adsorbates. The DFT-D3(BJ) procedure included dispersion corrections into the PBE functional for energies and gradients[27]. Molecular structures were optimized without geometrical constraints and verified through frequency analyses, where positive vibrations were associated with all vibrational modes. Convergence tolerance values of $1 \cdot 10^{-8}$ and $1 \cdot 10^{-6}$ Ha were used for SCF and geometry optimizations; the geometries converged with tolerance values in gradients and coordinate displacements of $3 \cdot 10^{-4}$ Ha/Bohr and $4 \cdot 10^{-3}$ Bohr, respectively. Continuum solvent effects were included by the universal continuum solvation model (SMD) based on the quantum mechanical charge density of a solute molecule interacting with a continuum description of the solvent[28]. Excited states were obtained with the simplified time-dependent density functional theory (sTD-DFT) approach combined with the meta-hybrid TPSSh functional (10% Hartree-Fock exchange)[29-30]; configuration state functions were included up to an energy threshold of 6.2 eV. Phosphorene nanoflakes ($P_{126}H_{30}$) were used for adsorption studies and with a surface area of at least ~1585 $Å^2$ considering its electron density, which is relatively larger to obtain well-converged adsorption energies concerning the fullerenes surface area (up to ~456 $Å^2$). Adsorption energies (E_{ads}) were computed as:

$$E_{ads} = E_{Phos} + E_{Fullerene} - E_{Phos-Fullerene} + \Delta ZPE \quad (1)$$

where E_{Phos}, $E_{Fullerene}$, and $E_{Phos-Fullerene}$ are the total energies of the free phosphorene, free fullerenes, and the complex, respectively; ΔZPE stands for the zero-point energy correction. Thus, the more positive the E_{ads} values, the more stable the complex is. The counterpoise correction was

used to avoid BSSE in the E_{ads} values[31]. Adsorption energies were further decomposed by the second-generation energy decomposition analysis based on absolutely localized molecular orbitals (ALMO-EDA) of the Q-Chem5.2 program at the PBE-D3/def2-TZVP level[32]. Hence, the adsorption energy for one AB complex expresses as[33-34]:

$$-E_{ads}=\Delta E_{CT}+\Delta E_{POL}+\Delta E_{ELEC}+\Delta E_{DISP}+\Delta E_{PAULI}+\Delta E_{PREP} \quad (2)$$

where ΔE_{CT}, ΔE_{POL}, ΔE_{ELEC}, and ΔE_{DISP} stand for the energy lowering due to charge-transfer (inter and intramolecular charge flow between fragments), polarization (induced electrostatics), Coulombic attractions (classical intermolecular electrostatics), and dispersion forces (van der Waals interactions), respectively. ΔE_{DISP} is obtained with the dispersion-free revPBE functional. ΔE_{PAULI} is the energy destabilization due to Pauli repulsion when two fragments are close enough, i.e., electrons cannot have the same position (Pauli principle). ΔE_{PREP} is the preparation energy penalty due to the geometric distortion of fragments to reach the complex geometry.

Intermolecular interactions were also revealed by the Atoms-in-Molecules (AIM) method[35], where the electron density (ρ_i) of the bond critical points (BCPs) connecting fragments through intermolecular bond paths serve as a measure of the interaction strength. In this way, covalent bonds, closed-shell interactions, and weak electrostatic interactions are characterized by ρ_i values of $\rho_i \geq 0.10$, $\rho_i \approx 0.10–0.04$, and $\rho_i \leq 0.01$ e/Bohr^3, respectively [35]. Furthermore, the signature of weak interactions were examined by the Independent Gradient Model (IGM)[36], which introduce the δg^{inter} descriptor that uniquely defines intermolecular interaction regions: $\delta g^{inter}=|\nabla\rho^{IGM,inter}|-|\nabla\rho|$, where $\nabla\rho$ stands for the electron density gradient and $\nabla\rho^{IGM,inter}$ is an upper limit to $\nabla\rho$ as defined by Lefebvre and co-workers[36]. AIM, IGM (based on the Hirshfeld partition), CM5 charges, and wavefunction analyses were performed in Multiwfn3.7[37].

3. Results and Discussions

3.1. Structure and stability.

We place fullerenes initially ~5 Å away from the phosphorene surface; at least ten orientations for each molecule were considered according to its symmetry. The **Phos–Fullerene** systems form two groups of stable complexes depending on the fullerene size (Fig. 1a): i) covalent and ii) non-covalent complexes. C_{24} to C_{44} fullerenes form covalent complexes with phosphorene *via* chemisorption, showing intermolecular distances of d_{inter}≈2.0–2.2 Å; while C_{50} to C_{70} fullerenes form non-covalent complexes *via* physisorption, showing intermolecular distances of d_{inter}≈2.6–2.8 Å (Fig. 1b).

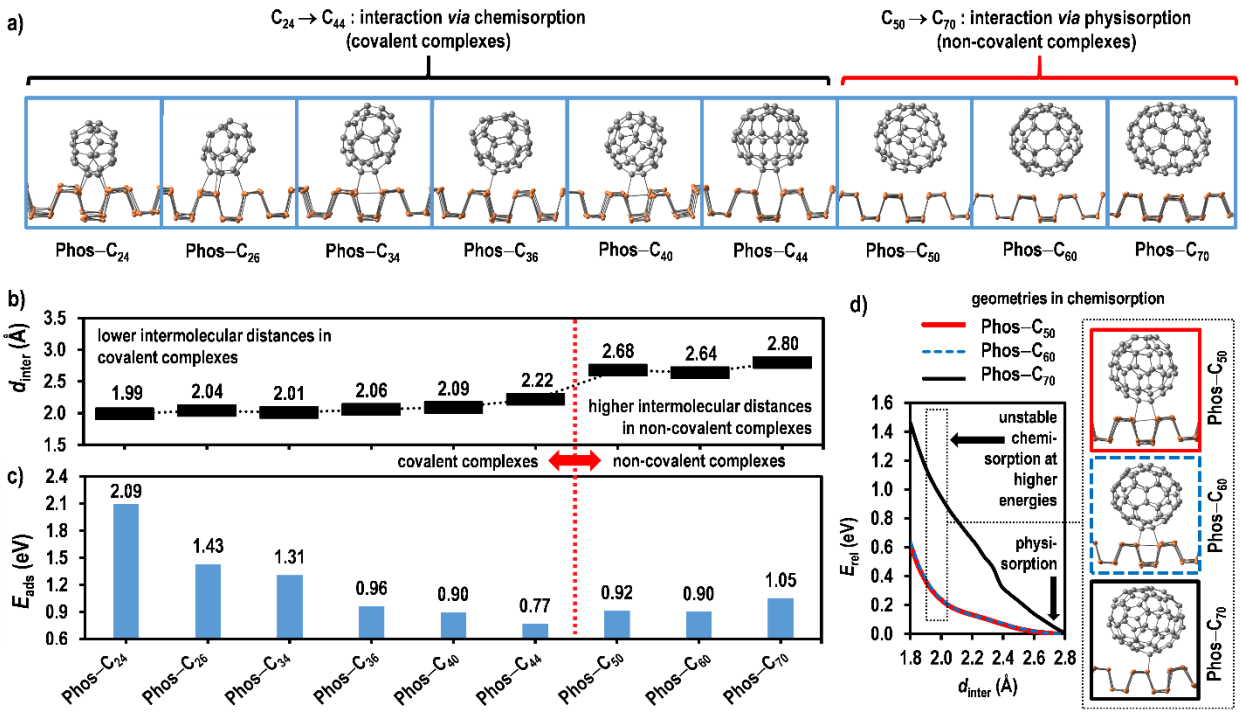

Fig. 1. Properties of **Phos–Fullerene** complexes: a) Ground state structures. b) Average intermolecular distances (d_{inter}, in Å). c) Adsorption energies of ground states (E_{ads}, in eV). d) Potential energy surface for the formation of covalent complexes at shorter intermolecular distances; the energy of the physisorbed state is set to zero.

In the case of the covalent complexes, the adsorption stability decreases as the size of fullerenes increases. C_{24}, C_{26}, and C_{34} form highly stable complexes, reaching positive adsorption energies of ~2.1, 1.4, and 1.3 eV, respectively (favorable adsorption, Fig. 1c). Interestingly, **Phos–C_{24}** and **Phos–C_{26}** complexes form a [4+4]-cycloaddition bonding, which compares to prototype graphene–fullerene hybrids called graphene nanobuds, where covalently bonded fullerenes or fusing fragmented C_{60} are designed onto a graphene monolayer *via* cycloaddition reactions[38-39]. Otherwise, C_{36}, C_{40}, and C_{44} reach relative medium stability upon adsorption, with positive adsorption energies of up to 0.9 eV (favorable adsorption). Structurally, C_{34}, C_{36}, C_{40}, and C_{44} fuse to phosphorene through cycloaddition of up [2+2] order, and adsorption energy decreases up to 67% compared to **Phos–C_{24}** and **Phos–C_{26}**.

On the other side, the C_{50}, C_{60}, and C_{70} fullerenes are physisorbed onto phosphorene with positive adsorption energies of up to 1.0 eV, denoting stable adsorption that compares to the stability reached by C_{36} and C_{40} *via* chemisorption (Fig. 1c). Note also adsorbed fullerenes could be further stabilized by neighboring molecules onto phosphorene through strong molecule-molecule interactions, arising two-dimensional self-assembly in the physisorption regime as reported for C_{60} adsorption[19]. Compared to our results, periodic vdW-KBM calculations and molecular dynamics simulations have reported non-covalent **Phos–C_{60}** complexes with E_{ads} values of ~0.7 and ~–1.0 eV, respectively[19, 23]; then, our results agree with previous reports. Additionally, UV-VIS-NIR absorbance, temperature scanning tunneling microscopy, and scanning tunneling spectroscopy measurements indicate that C60 molecules physically adsorb on phosphorene, where desorption occurs with annealing 400 K[20-21]. As can be seen, E_{ads}=~0.9 eV for **Phos–C_{60}** complexes agrees with the experimental favorable non-covalent adsorption of fullerenes on phosphorene-based materials. Furthermore, the C_{60} adsorption stability increases at least 30%

compared to related 2D materials such as graphene, where E_{ads}≈0.7 eV is reported for Graphene–C_{60} non-covalent complexes[40-44]. Therefore, phosphorene serves as excellent support for fullerenes to form new hybrid nanostructures, ensuring a stable interaction.

We also compute the potential energy surface (PES) of non-covalent complexes to search for possible states where chemisorption occurs (Fig. 1d). PES begins at intermolecular distances of d_{inter}≈2.8 Å, where the physisorption state is set to zero. The non-covalent complexes turn into covalent complexes at d_{inter}≈2.0 Å, reaching [2+2]-cycloaddition configurations. Nevertheless, covalently bonded states do not reach saddle points in the PES, even without energy barriers. The latter indicates that PES is repulsive for d_{inter}<2.8 Å, denoting chemisorption is unstable for **Phos–C_{50}**, **Phos–C_{60}**, and **Phos–C_{70}** complexes. In other words, covalently bonded metastable states will have a short lifetime and poor stability due to the lack of dissociation barrier to reach the non-covalent states. This behavior is different from graphene and carbon nanotubes, where C_{60} fullerenes reach highly stable chemisorbed states at room temperature due to the relatively high dissociation barrier to reach the physisorbed states ($\Delta E^{\neq}$>0.7 eV)[39, 45]. The absence of an energy barrier to reach chemisorbed states is a consequence of phosphorene nonplanarity due to its shape of structural ridges; in contrast, the chemical Graphene–C_{60} attachment requires a high energy barrier due to the lack of local puckering in the graphene structure[39, 41].

Regarding stability in solvent media, almost all **Phos–Fullerene** complexes) show high stability in different solvents, independent of the solvent polarity (Fig. 2). In this way, solvation energies cause a slight penalty in the adsorption energies (~30%). The exception is the **Phos–C_{44}** and **Phos–C_{70}** complexes, whose stability is decreased up to 96% in high/medium polar solvents

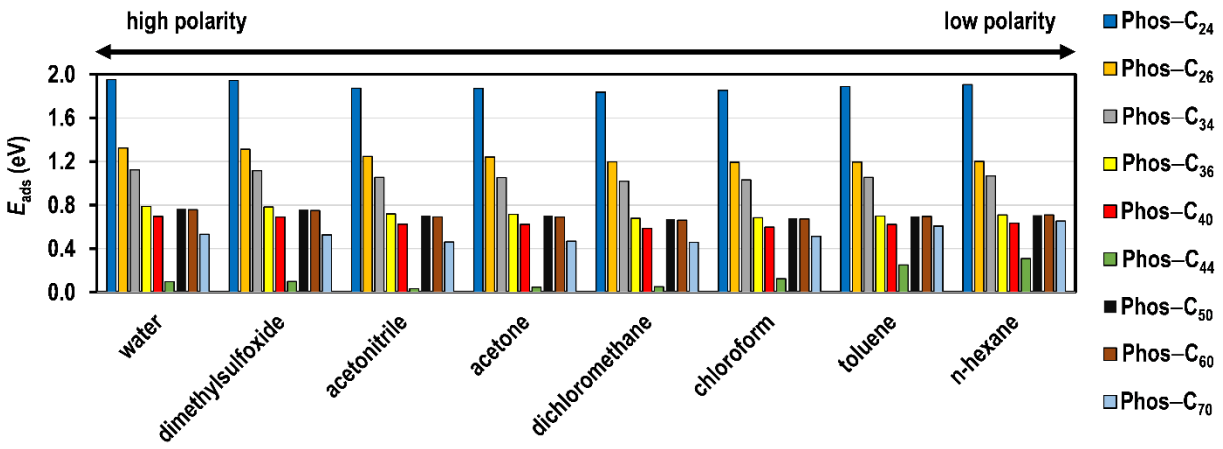

Fig. 2. Adsorption energies of the **Phos–Fullerene** complexes in solvents (E_{ads}, in eV).

due to differences in solute-solvent polarity with respect to the free fragments. Consequently, solvents with low dielectric constants would be adequate for **Phos–C_{44}** and **Phos–C_{70}** dilution, e.g., toluene and n-hexane. Another key point to emphasize, phosphorene can be sensitive and oxidized underwater and oxygen conditions[46]. However, phosphorene oxidation does not imply that fullerene adsorption will be hindered, and new synthetic techniques are developed to improve the stability of phosphorene layered materials for several applications[47-48]. Despite the latter, recent reports highlight the physisorption of C_{60} during an assembly at the air-water interface contribute to protecting phosphorene thin films from oxidation and inhibiting the overlapping stacking or agglomeration of phosphorene nanosheets in solvents[20].

3.2. Electronic properties.

Relevant electronic properties of the **Phos–Fullerene** complexes are displayed in Table 1. In terms of charge distribution, all systems show electron transfer in the Phos→Fullerene direction. The negative charge on fullerenes after interaction (Q_{full}) is of the order of ~–0.1 to –0.3|e| for covalently bonded fullerenes (C_{24}–C_{44}), while physisorbed fullerenes gain up to ~0.1|e| (C_{50}–C_{70}). Consequently, carbon fullerenes act as mild *p*-dopants for phosphorene, introducing up to ~0.3

holes/molecule on the substrate. Moreover, carbon, boron, boron nitride, and silicon carbide fullerenes have also behaved as *p*-dopants upon adsorption on related 2D materials such as pristine graphene and metal-doped graphene[40, 42, 49-50].

The electron transfer in the Phos→Fullerene direction for all the complexes is consistent with the chemical potential (μ) of the fragments (Table 1): μ characterizes the response of the system energy with respect to changes in the electron number, thus related to the electronegativity χ through $\mu=-\chi$[51]. Hence, electrons move from the system with high chemical potential (phosphorene, μ=-4.4 eV) to the one with low chemical potential (fullerenes, μ=-4.7 to -5.3 eV) for establishing new electronic equilibrium. Further, we found the low energy of the HOMO level of fullerenes avoids the electrons to flow from the HOMO of fullerenes to the phosphorene conduction band. In the same fashion, Wang and co-workers found *via* photoelectron spectra measurements that electrons are transferred from phosphorene to C_{60}, where it is experimentally

Table 1. Electronic properties of the Phos–Fullerene systems: CM5 charge of fullerenes (Q_{Full}, in $|e|$); Chemical potential (μ, in eV); Molecular dipole moment (μ_D, in Debye); Isotropic first electric dipole polarizabilities (α, in $1\cdot10^{-22}$ esu); HOMO and LUMO energies, and HOMO-LUMO energy difference (ε_{HOMO}, ε_{LUMO}, and Δ_{HL}, respectively, in eV); Percentage of change of Δ_{HL} with respect to free phosphorene (%$\Delta\Delta_{HL}$, in %).

Systems	Q_{full}	μ	μ_D	α	Δ_{HL}	%$\Delta\Delta_{HL}$
Phos–C_{24}	-0.08	-5.0[a]	0.73	6.47 (0.30)[c]	0.49 (0.42)[d]	61
Phos–C_{26}	-0.28	-5.1[a]	4.34	6.60 (0.33)[c]	0.28 (0.40)[d]	78
Phos–C_{34}	-0.10	-5.0[a]	1.88	6.62 (0.43)[c]	0.35 (0.47)[d]	73
Phos–C_{36}	-0.21	-4.7[a]	3.16	6.66 (0.45)[c]	0.31 (0.41)[d]	75
Phos–C_{40}	-0.12	-5.1[a]	1.17	6.65 (0.49)[c]	0.57 (0.85)[d]	56
Phos–C_{44}	-0.14	-5.3[a]	1.48	6.69 (0.55)[c]	0.45 (0.75)[d]	64
Phos–C_{50}	-0.07	-5.2[a]	1.16	6.81 (0.66)[c]	0.76 (1.32)[d]	40
Phos–C_{60}	-0.06	-5.0[a]	0.86	6.88 (0.76)[c]	1.06 (1.65)[d]	17
Phos–C_{70}	-0.03	-5.0[a]	0.47	7.01 (0.95)[c]	1.10 (1.70)[d]	14
Phos	-	-4.4[b]	-	6.17	1.27	

[a]μ values of free fullerenes. [b]μ value of free phosphorene. μ is obtained as $\mu=(\varepsilon_{HOMO}+\varepsilon_{LUMO})/2$, where ε_{HOMO} and ε_{LUMO} are the eigenvalues of the HOMO and LUMO, respectively. [c]Polarizability of free fullerenes. [d]Δ_{HL} of free fullerenes.

noted that work function of C_{60} (WF≈5.7 eV) is considerably higher than the ionization potential of phosphorene (IP≈4.2 eV). Note that in the Koopmans' Theorem scheme, $WF \approx IP \approx -\varepsilon_{HOMO}$; thus, the HOMO level of C_{60} must be lower in energy concerning the Fermi level of phosphorene[22], in agreement with our results.

As well the sites accumulating electrons after interaction were studied by the electron density difference [$\Delta\rho$(r)], where yellow and red regions denote accumulation and depletion of electron density, respectively (Fig. 3a-c). For the covalent complexes (e.g., **Phos–C$_{24}$** and **Phos–C$_{40}$**, Fig. 3a-b), there is a strong electron accumulation at the bonded carbon atoms of fullerenes, which is also accumulated in their surrounding C–C bonds. While electron depletion mainly comes from the interacting 3*p* lone-pair orbitals of P atoms in the substrate. These results suggest the holes remain localized in specific sites of the phosphorene after electron transfer and in the absence of external bias potential. The non-covalent complexes (e.g., **Phos–C$_{60}$**, Fig. 3c)

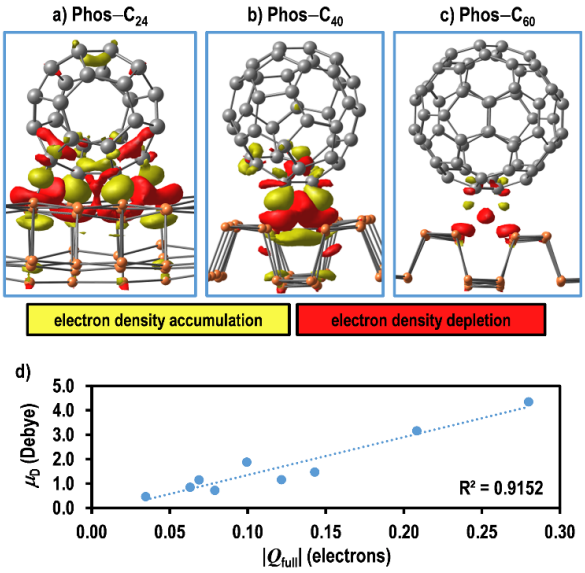

Fig. 3. a-c) Electron density difference [$\Delta\rho$(r)] of representative **Phos–Fullerene** complexes. Yellow and red densities stand for accumulation or depletion of electron density after the interaction, respectively. d) Dipole moment (μ_D) vs magnitude of fullerene charge ($|Q_{Full}|$) of all the **Phos–Fullerene** complexes.

displays an analogous $\Delta\rho(r)$ pattern but with a low magnitude due to the weak electron-transfer. The electron density rearrangements also induce dipole moments in the range of ~0.5–4.3 Debye (μ_D, Table 1); note all free systems are non-polarized in their free states ($\mu_D \approx 0$). The induced dipole moments show a directly proportional correlation to the charge transfer magnitude (Fig. 3d). Also, dipole polarizability α of the complexes increases compared to free phosphorene ($\alpha > 6.47 \cdot 10^{-22}$ esu vs. $6.17 \cdot 10^{-22}$ esu, Table 1), denoting an improving ability to acquire an electric dipole moment in proportion to external perturbations such as an electric field. Likewise, the polarizability of complexes increases as the polarizability of free fullerenes increases, which is directly proportional to the electron density volume of fullerenes.

Considering that electron transfer could be responsible for changes in the substrate energy levels because of the charge doping, we analyze the bandgap of the systems (Table 1). The HOMO-LUMO energy difference (Δ_{HL}) of intrinsic phosphorene is ~1.3 eV, denoting its semiconductor character as reported from previous first-principles calculations (~1.4–1.5 eV)[52-53]. Conversely, carbon fullerenes show Δ_{HL} values in the range of 0.4 to 1.7 eV, which increase as their size increases (see parenthesis in Table 1). Upon interaction, Δ_{HL} values of **Phos–Fullerene** nanostructures decrease up to ~1.0 eV (78%) with respect to intrinsic phosphorene, this is increasing the metallic character. The covalent adsorption of fullerenes causes a larger decrease in the bandgap (56–78%). Nevertheless, we can establish a more general relation:

- Small energy-bandgap fullerenes ($\Delta_{HL} < 0.8$ eV, typified by C_{24} to C_{50}) largely increase the phosphorene metallic character.
- Medium energy bandgap fullerenes ($\Delta_{HL} > 0.8$ eV, typified by C_{50} to C_{70}, and possibly the bigger ones) slightly increase the phosphorene metallic character.

In the final analysis, deposition of small fullerenes could be an efficient strategy for modulation of phosphorene bandgap *via* molecular doping, i.e., increasing its metallic character. The bandgap modulation mechanism is mainly due to LUMO stabilization and HOMO destabilization for **Phos–C$_{24}$** to **Phos–C$_{40}$** complexes because of the high charge transfer (Fig. 4). In the case of complexes **Phos–C$_{44}$** to **Phos–C$_{70}$**, the bandgap decreasing emerges due to stabilization of the LUMO level of phosphorene. Considering related 2D materials such as graphene, the fullerene adsorption induces bandgap opening of ~0.3-0.4 eV[54-55], which is due to the stress/strain externally exerted by fullerenes on the substrate structure[56]. Therefore, we can conclude bandgap modulation in phosphorene could result from charge transfer and/or stress-strain effects exerted upon fullerene attachment. About the reliability of these results, periodic DFT calculations have predicted bandgap values of ~1.0 eV for **Phos–C$_{60}$** complexes[23], which agrees with this work (Δ_{HL}=1.1 eV for **Phos–C$_{60}$**). Moreover, we compute bandgap values of ~1.7 eV for C_{60} and C_{70}, which agree with those reported via photothermal deflection spectra and temperature-dependent microwave conductivity measurements[57-58]: 1.6-1.8 eV (C_{60}) and 1.6 eV (C_{70}). The latter ensures the reliability of the employed theoretical methodology.

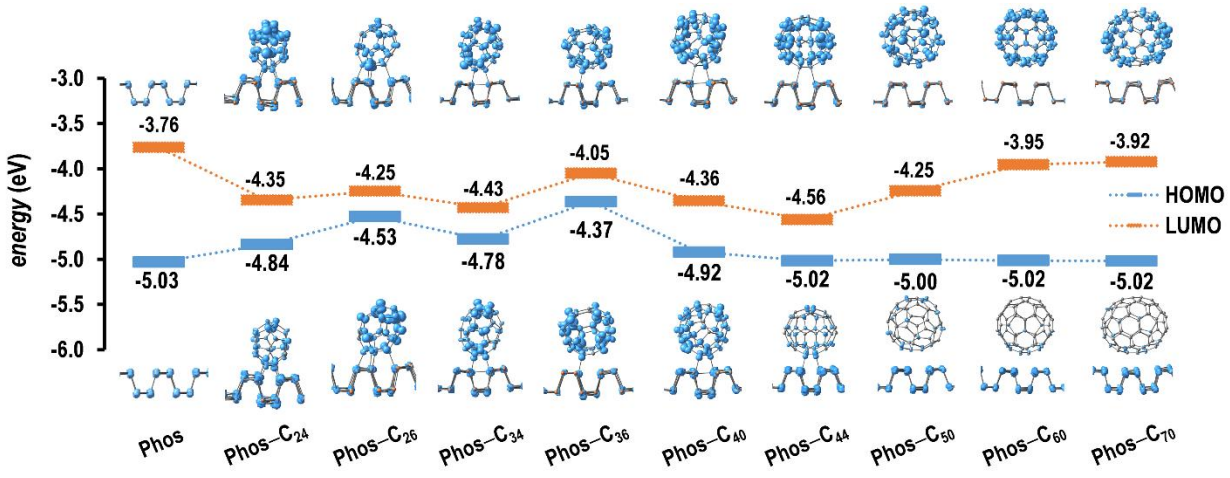

Fig. 4. HOMO and LUMO energies of Phos–Fullerene complexes. HOMO and LUMO densities are displayed below and above, respectively; isosurface value of 0.003 a.u.

Regarding the topology of frontier molecular orbitals in the complexes (Fig. 4), covalent complexes show the HOMO located in both phosphorene and fullerene moieties due to the orbital interactions. However, the fullerene contribution to the HOMO decreases as the chemical bonding character decreases until it almost disappears in non-covalent complexes. Conversely, LUMO is almost entirely located in fullerene for all the complexes. Thus, fullerenes act as active sites for orbital-controlled interactions, mainly retaining their donor/acceptor properties when chemisorbed on phosphorene. While fullerene mainly will act as acceptor sites when physisorbed on phosphorene.

3.3. Interaction mechanism.

We provide a quantitative and readily physical interpretation of the adsorption mechanism by examining the specific role of the stabilizing effects into the adsorption energies and employing the EDA method. The attention is focused on the stabilizing contributions of Eq. (2) (ΔE_{CT}, ΔE_{POL}, ΔE_{ELEC}, ΔE_{DISP}) because destabilizing terms were up to 95% only due to Pauli repulsion (ΔE_{PAULI}). For a standardized interpretation among systems, relative single percentage contributions of EDA terms are discussed (%ΔE_i, Fig. 5a).

First, the stability of covalent complexes (**Phos–C$_{24}$** to **Phos–C$_{44}$**) emerges from the charge-transfer term (ΔE_{CT}) because of the strong orbital interactions with a contribution of ~38-48% to the stabilizing energy (Fig. 5a), agreeing with the high magnitude of electron transfer in the covalent complexes (Table 1). The second highest contribution to the stability emerges from polarization effects as expected in short-range orbital interactions (ΔE_{POL}, up to 32%). The latter denotes strong intramolecular charge rearrangements due to the on-fragment relaxation of each species to the presence of the nuclei and electrons of all other fragments. Then, covalent bonding

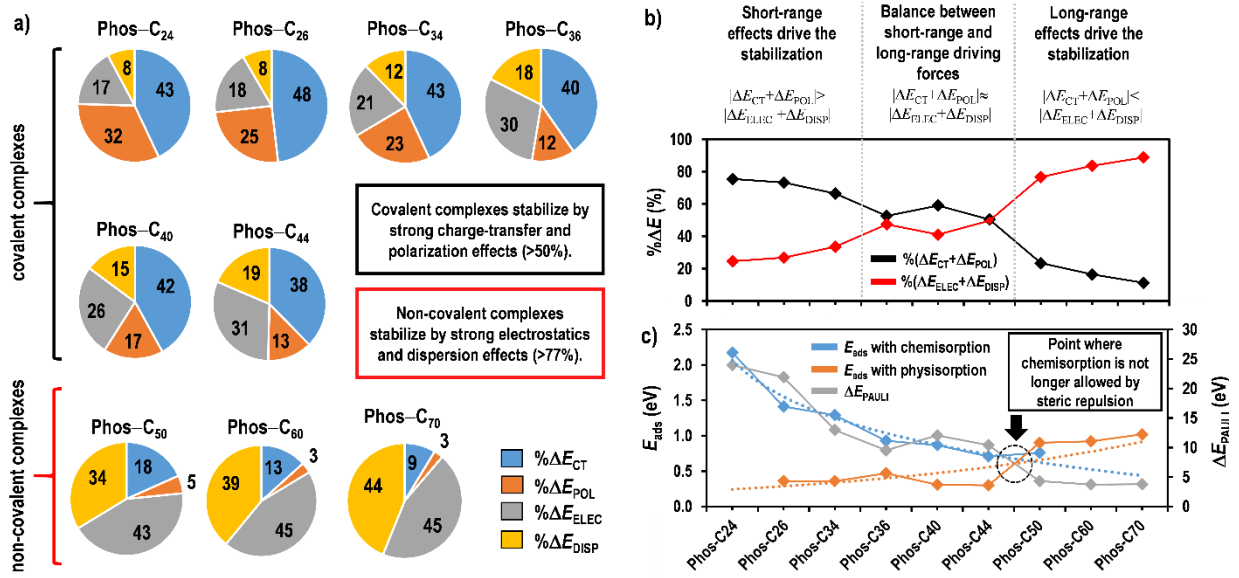

Fig. 5. Energy decomposition analyses: **a)** Relative single percentage contributions (%ΔE_i, in %) of stabilizing terms. **b)** Comparison between combined percentual contributions of short-range (ΔE_{CT}+ΔE_{POL}) and long-range (ΔE_{ELEC}+ΔE_{DISP}) terms. **c)** Adsorption energies (E_{ads}, in eV) upon chemisorption and physisorption vs. steric repulsion energy (ΔE_{PAULI}, in eV); a physisorption configuration cannot be obtained for the **Phos–C$_{24}$** complex; while **Phos–C$_{50}$**, **Phos–C$_{60}$**, and **Phos–C$_{70}$** only shows stable physisorption configurations.

is demonstrated from the physical viewpoint. It is worth mentioning that an obvious correlation between the number of transferred electrons and ΔE_{CT} magnitude cannot be established because ΔE_{CT} term also accounts for energy lowering associate with intramolecular electron flow, allowing to delocalize electrons over the complex. The latter explains why the ΔE_{CT} contribution is high in **Phos–C$_{24}$** (43%) in spite that the whole intermolecular charge transfer is low (~0.08|*e*|, Table 1), which could be caused by strong intrafragment electron density rearrangements and bond polarization in the [4+4]-cycloaddition as noted from the high ΔE_{POL} contribution (32%).

The AIM analysis allows assessing the binding mechanism from the values of electron density (ρ_i) at intermolecular bond critical points [BCPs, points in space at which the first derivatives of the electron density vanish $\nabla\rho(r)=0$, Fig. 6]. Accordingly, the covalent complexes

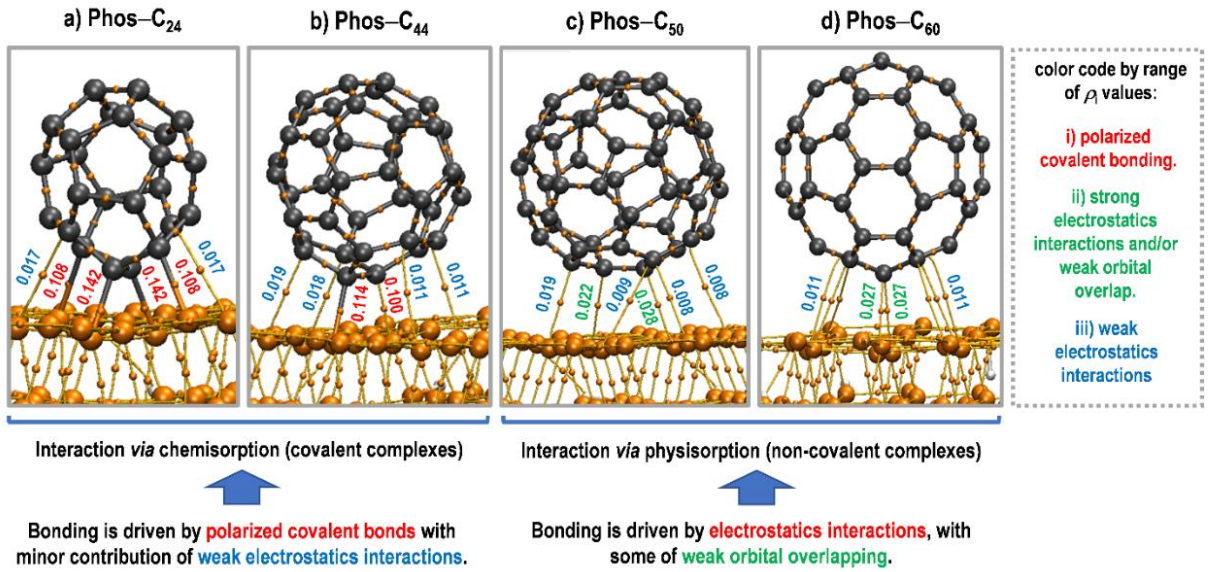

Fig. 6. Electron density at the bond critical points of intermolecular interactions (ρ_i, in e/Bohr^3) for representative Phos–Fullerene complexes.

reveal short-range intermolecular C–P bonding with ρ_i values of $\rho_i \approx 0.10–0.14$ e/Bohr^3, which associate to polarized covalent bonding by sharing electrons (red numbers in Fig. 6a-b). Natural bond orbital analyses (NBO) reveal at least 60% of the C–P bond density is polarized to fullerene carbon atoms due to their strong acceptor character. Therefore, the polarized covalent bonding in covalent complexes agrees with the high ΔE_{CT} and ΔE_{POL} contributions. In the molecular orbital picture, the bonding occurs when interacting carbon atoms of fullerenes hybridize from $sp^2 \rightarrow sp^3$, forming σC–P polarized covalent bonds with the low-occupied lone-pair 3p orbitals of phosphorus atoms in the substrate. Additionally, BCPs appear at long-range C–P interactions ($\rho_i \leq 0.02$ e/Bohr^3), which are associated with weak electrostatic interactions (blue numbers in Fig. 6a-b). In this regard, EDA shows the electrostatic term (ΔE_{ELEC}) reaches the third largest contribution to the stability (17-31%). The electrostatic contribution emerges from the electron-sufficient carbon atoms of fullerenes, which acquire a negative charge that electrostatically attracts the electron-

deficient phosphorous atoms of phosphorene as noted from electron density rearrangements [see the $\Delta\rho$(r) surface, Fig. 3a-c].

It is necessary to note ΔE_{CT} and ΔE_{POL} contributions mainly decay as the intermolecular distances increase due to the connection to orbital overlap, becoming ΔE_{CT} and ΔE_{POL} mostly short-range terms. In that case, the combined contribution of short-range terms defines two classes of covalent complexes (Fig. 5b):

i. Members of the first class (typified by **Phos–C$_{24}$**, **Phos–C$_{26}$**, **Phos–C$_{34}$**) have short-range terms influencing the magnitude of adsorption energies, which highly contribute compared to long-range terms (electrostatics and dispersion): $\Delta E_{CT}+\Delta E_{POL}>\Delta E_{ELEC}+\Delta E_{DISP}$.

ii. The second class of covalent complexes is represented by **Phos–C$_{36}$**, **Phos–C$_{40}$**, and **Phos–C$_{44}$**, where a balanced contribution of long-range and short-range driving forces determine the magnitude of adsorption energies: $\Delta E_{CT}+\Delta E_{POL}\approx\Delta E_{ELEC}+\Delta E_{DISP}$.

In the framework of steric effects, we can establish that a relatively larger volume of fullerenes (C_{36}, C_{40}, C_{44}) would cause a larger steric repulsion at shorter intermolecular distances in the second class of complexes. In this manner, intermolecular distances slightly increase ($d_{inter}\approx$2.1–2.2 Å) to compensate for the volume exclusion effects when fragments are brought into close interaction. As a result, the strong stabilization gained by short-range contributions decay and weak long-range E_{ELEC} and ΔE_{DISP} effects compensate the steric destabilization; consequently, lower adsorption energies are reached compared to the first class of covalent complexes (Fig. 1b).

Focusing now on non-covalent complexes (**Phos–C$_{50}$**, **Phos–C$_{60}$**, and **Phos–C$_{70}$**), the stabilizing part of the adsorption energy mainly arises from permanent Coulombic electrostatic and dispersion driving forces ($\Delta E_{ELEC}+\Delta E_{DISP}$, up to 90%, Fig. 5a). In this regard, the minimization

of dispersion and electrostatic interactions also plays a key role in forming organic molecular crystals, phthalocyanine self-assemblies, and DNA nucleobase patterns onto phosphorene-based substrates, standing for ~85% of the stability[19, 59-61]. It can be pointed out although phosphorene is not a π-electron system, it behaves with a similar attractive ability than graphene or carbon nanotubes to bind aromatic molecules, where fullerenes adsorb by π-π stacking[39-45]. In this regard, the 3D δg^{inter} isosurface representation of weak intermolecular interactions is visually displayed for **Phos–C$_{60}$** complex as a representative case and compared against **Graphene–C$_{60}$** (Fig. 7a). The weak interaction pattern shows a similar shape in both **Phos–C$_{60}$** and **Graphene–C$_{60}$**, so dispersion forces (green regions) play a key role in both systems. This ability arises because of the larger amount of 3*p* lone pair electrons in the phosphorene upper lattice, which can correlate with the π-electrons of aromatic molecules and cause transitory induced dipoles responsible for dispersion forces[61].

Additionally, δg^{inter} pattern shows that polar interactions (blue regions) have a higher intensity on phosphorene compared to graphene, denoting the major role of electrostatic driving

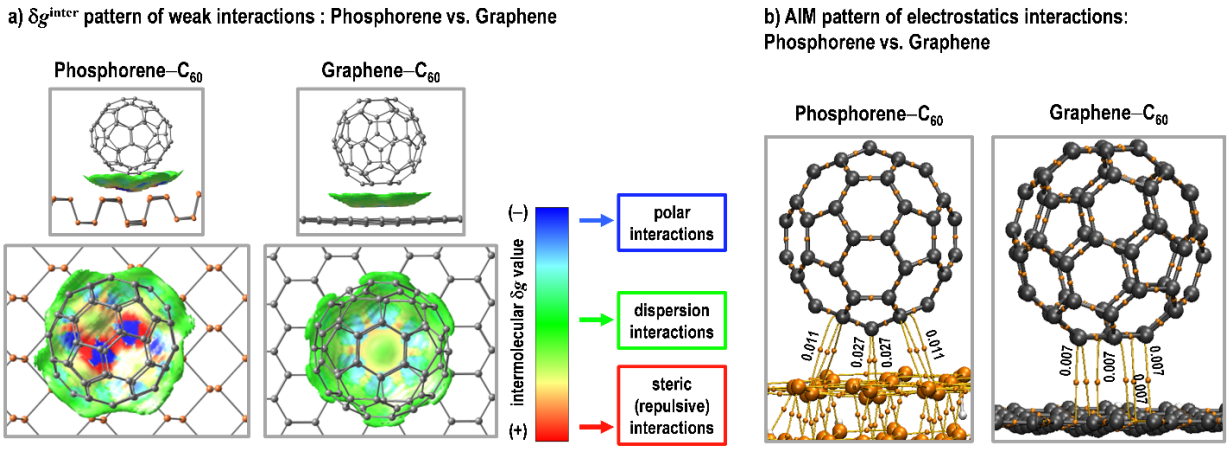

Fig. 7. Properties of **Phosphorene–C$_{60}$** vs. **Graphene–C$_{60}$** nanostructures: a) δg^{inter} isosurface of weak interactions; b) Electron density at the bond critical points (ρ_i, in *e*/Bohr^3).

forces for C_{60} stabilization onto phosphorene (Fig. 7a). According to AIM analyses, non-covalent complexes displays two type of electrostatic interactions (Fig. 6c-d): **i**) weak electrostatics interactions at longer distances, typified by $\rho_i \leq 0.02$ *e*/Bohr^3 (blue numbers); **ii**) strong electrostatic interactions, typified by $\rho_i \approx 0.02\text{-}0.03$ *e*/Bohr^3 (green numbers). The NBO analysis also reveals strong electrostatics interactions involve a weak orbital overlapping due to electron donation from phosphorene 3*p* lone pairs towards low-occupied π*C–C orbitals of fullerenes, while fullerenes show back-donation from single-occupied 2*p* orbitals towards unoccupied σ*P–P bonds of the substrate. When compared against the **Graphene–C$_{60}$** complex, AIM analyses also show electrostatics interactions are favored in the **Phos–C$_{60}$** case with lower electron density values for the former ($\rho_i \leq 0.01$ *e*/Bohr^3, Fig. 7b). These results clarify how electrostatics driving forces favor the adsorption onto phosphorene with respect to related 2D materials. For instance, the **Phos–C$_{60}$** system shows ΔE_{ELEC} and ΔE_{DISP} contributions of 45 and 39%, respectively (major contribution of electrostatics, Fig. 5a); while the **Graphene–C$_{60}$** system is reported with ΔE_{ELEC} and ΔE_{DISP} contributions of 33 and 67%, respectively (major contribution of dispersion)[40].

Otherwise, ΔE_{CT} and ΔE_{POL} terms show low stabilizing contributions in the non-covalent complexes because they are mainly short-range terms. Specifically, ΔE_{CT} shows a slightly larger contribution than ΔE_{POL}, with a contribution of up to 18% (**Phos–C$_{50}$**). ΔE_{CT} contribution in these cases relates to the donor-acceptor orbital interactions as noted above: donation 3*p*(**Phos**)→π*C–C(**Fullerene**), and back-donation 2*p*(**Fullerene**)→σ*P–P(**Phos**). In this way, ΔE_{CT} contributions decrease as the number of transferred electrons decreases.

Additionally, the choice of either covalent or non-covalent configurations can also be elucidated based on steric effects. Fig. 5c displays the adsorption energies and considering

chemisorption and physisorption adsorption configurations when possible. First, complexes **Phos–C$_{24}$** to **Phos–C$_{40}$** prefer to bind by covalent bonding, i.e., E_{ads}(chemisorption)>E_{ads}(physisorption); consequently, although covalent complexes can reach a stable physisorption state, the chemisorption will be thermodynamically preferred. Also, Fig. 4c displays the Pauli repulsion energy (ΔE_{PAULI}) in the most stable adsorption configurations. Accordingly, covalent complexes show high ΔE_{PAULI} values, but the charge-transfer and polarization effects overcompensate the Pauli repulsion ($\Delta E_{CT}+\Delta E_{POL}>\Delta E_{PAULI}$), leading to stable adsorption. Note that as the fullerene size increases, the intermolecular distance increases to compensate for the repulsion energy. The energy penalty emerges as kinetic energy pressure exerted by electrons when atoms are brought into close interaction[34]. As a result, the ΔE_{PAULI} term decreases as the adsorption energy decreases until the **Phos–C$_{44}$** complex. In other words, we found at this point the fullerene size at which chemisorption is no longer allowed, which is set between C_{44} and C_{50} (Fig. 5c). This limit arises because the intermolecular separations must increase to decrease the repulsion energy; consequently, physisorption is a stable state at longer intermolecular distances for bigger fullerenes (C_{50}, C_{60}, and C_{70}). Therefore, ΔE_{PAULI} is the primary driving force that compensates all the stabilizing effects to establish the energetically optimal intermolecular separation between phosphorene and fullerenes.

Finally, destabilizing terms mainly arise from Pauli repulsion; however, the covalent complexes involve geometrical preparation energies ΔE_{PREP} due to the required orbital hybridization $sp^2 \rightarrow sp^3$ of fullerenes and rearrangements of phosphorene sublattices, which equals to contributions of 10–16% to the destabilizing energy. The root-mean-square deviation RMSD of the fullerene geometries in the complex ranges from 0.04 to 0.94 Å with respect to the free

molecules, which increase with the order of cycloaddition reaction. Although there is an energy penalty due to weak structural changes to reach the covalent bonding, the low RMSD values show that the electronic/structural rearrangements are low-scale and are not prohibited.

3.4 Outlook of Phos–Fullerene nanostructures.

This work provides a first pivotal stepping-stone to exploring the immense possibilities of the proposed nanostructures in future theoretical/experimental studies. All analyses considered, in addition to comparisons with related hybrid structures, show some interesting potential uses for **Phos–Fullerene** nanostructures. For instance, covalent **Phos–Fullerene** complexes display a graphene nanobud-like structure and strong electron transfer in the Phos→Fullerene direction. In this regard, graphene nanobuds have shown potential uses in energy and gas storage devices with high stability at room temperature, new spintronics, position sensing, and graphene band structure engineering[38-39, 54, 62]. Furthermore, Li adsorption was enhanced for graphene–C_{60} nanobuds by the high electron affinity of C_{60} and the charge transfer from graphene to C_{60}[55, 63]. Accordingly, the strong charge transfer in the Phos→Fullerene direction turns covalent complexes into remarkable candidates to be studied as novel storage and anode materials in Li/Na-ion battery applications.

Additionally, orbital analyses show that fullerenes act as active sites for orbital-controlled interactions, mainly retaining their donor/acceptor properties when chemisorbed on phosphorene. While fullerene mainly will act as acceptor sites when physisorbed on phosphorene. Also, fullerenes increase the metallic character of phosphorene. The latter suggest fullerenes could act as signal amplifiers for specific redox applications considering that phosphorene-based materials have shown interesting electrochemical performance as electrode materials. Deposited mesoporous and organic molecules have caused effective signal amplification on phosphorene-

based sensors to determine prostate-specific antigen, hemoglobin, clenbuterol, and polychlorinated biphenyls, reaching an excellent specificity, chemical stability, low detection limits, and reproducibility[64-66]. The electrochemical amplification mechanism emerges from the good charge transfer in the hybrid material, an enhanced electrical conductivity of the electrode, and the excellent electrocatalytic activity of the deposited molecules upon adsorption[65]. Therefore, our results open avenues for the study of **Phos–Fullerene** hybrids in electrochemical biosensing.

On the other hand, charge-doping and bandgap changes reveal phosphorene conductance can be tailored by deposition of fullerenes. Since the bandgap value is directly proportional to the conductance ($\sigma \propto \Delta_{HL}/kT$, where k is the Boltzmann constant and T the temperature), our results define a framework to explore the charge-transport and optoelectronic response of **Phos-Fullerene** nanostructures. As an illustration, the increased charge transport of graphene due to C_{60} deposition[54-55], and the strong electron-accepting characteristics of C_{60} causing a hole-doped nature in graphene, lead to hybrid structures allowing photogenerated carriers for high-performance photodetector devices[50]. It is also noticed that a larger electron transfer in the Phos→Fullerene direction is responsible for lower bandgap values, resulting in a higher conductance. In this way, functionalized fullerenes with strong acceptor functional groups could be implemented to maximize the electron transfer and charge transport.

Furthermore, small bandgaps would enable UV-Vis radiation absorption by Phos–Fullerene nanostructures as required for optoelectronic applications. In fullerene-based polymer solar cells, phosphorene has enabled a strong absorption between 300-800 nm and better energy alignment in the device layers, which is significantly beneficial to the charge transfer, exciton dissociation, and reduce charge recombination, consequently enhancing the power

conversion efficiency[18]. In addition, C_{60} allowed absorption in the visible range for mm-scale heterojunction phosphorene-based photodetectors, where synergistic effects enable high photoresponse from the visible to near-infrared spectrum[20]. Accordingly, synergistic properties of **Phos–Fullerene** complexes could inspire experimental/theoretical studies on its uses for future generation solar energy harvesters or as active layers within photodetector devices. To support these points, we verified the UV-Vis spectrum of the proposed nanostructures in n-hexane as a solvent commonly implemented to study the fullerene absorbance (Fig. 8). Intrinsic phosphorene shows a wide absorbance from the infrared, which increases in intensity below 500 nm as recorded from UV–vis spectrophotometry[67]. In comparison, most free fullerenes absorb high molar absorption coefficients at the UV region below λ_{abs}<400 nm (Fig. 5a). **Phos–Fullerene** nanostructures almost resemble the absorption spectra of free phosphorene (Fig. 5b), but a remarkably improved absorption at higher frequencies is reached (λ_{abs}≈400-500 nm). Then, fullerenes maximize the phosphorene absorbance at the UV-Vis region, denoting the emerging synergistic effects for optoelectronics and photodetectors.

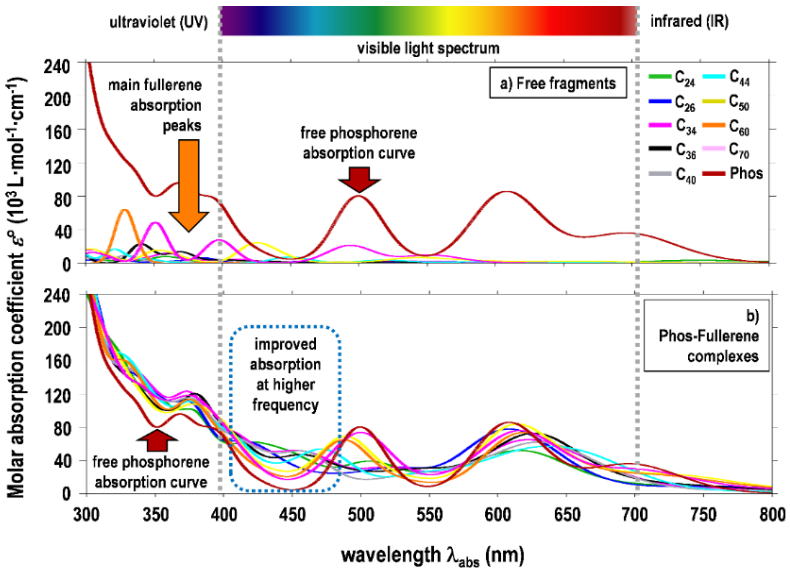

Fig. 8. Absorption spectra of **a)** free phosphorene and fullerenes; **b)** Phos–Fullerene complexes.

4. Conclusions

We have computationally elucidated the structure, stability, and interaction mechanisms of phosphorene-fullerene nanostructures, which form covalent and non-covalent complexes depending on the fullerene size and outstanding stability compared to related 2D materials, even in solution. Two classes of covalent complexes arise by cycloaddition-like reactions of up to [4+4] order: the first class (C_{24}–C_{34}), where short-range stabilizing effects dominate; and the second one (C_{36}–C_{44}), where short-range effects decay to avoid steric repulsion, and balanced long-range forces favor the stability. High-size fullerenes (C_{50}–C_{70}) form non-covalent complexes due to strong repulsion at shorter intermolecular distances and lack of dissociation barriers. Furthermore, fullerenes act as mild *p*-dopants for phosphorene, increasing its polar character and ability to acquire induced dipole moments (polarizability). Also, small energy-bandgap fullerenes (<0.8 eV) largely increase the phosphorene metallic character. We also note fullerenes retain their donor/acceptor properties upon adsorption, acting as active sites for orbital-controlled interactions and maximizing the phosphorene absorbance at the UV-Vis region. Future work should focus on relevant applications of the proposed nanostructures for storage, anode materials in Li/Na-ion batteries, electrochemical sensing, bandgap engineering, and/or optoelectronics.

Acknowledgments

The authors thank the financial support and computational resources through projects ANID/FONDECYT 1210355, ANID/PAI PAI77200068, and ANID-FONDEQUIP EQM180180. Powered@NLHPC: This research was partially supported by the supercomputing infrastructure of the NLHPC (ECM-02). There are no competing interests to declare by the authors of this article.

References

1. Chen, M.; Guan, R.; Yang, S., Hybrids of Fullerenes and 2d Nanomaterials. *Adv. Sci.* **2019**, *6*, 1800941.
2. Kharlamov, A.; Kharlamova, G.; Bondarenko, M.; Fomenko, V., Joint Synthesis of Small Carbon Molecules (C3-C11), Quasi-Fullerenes (C40, C48, C52) and Their Hydrides. *Chem. Eng. Sci.* **2013**, *1*, 32-40.
3. Goel, A.; Howard, J. B.; Vander Sande, J. B., Size Analysis of Single Fullerene Molecules by Electron Microscopy. *Carbon* **2004**, *42*, 1907-1915.
4. Mirzaie, A., A Density Functional Theory Study on the Effect of Size on the Ionization Potential of Different Carbon Fullerenes. *J. Med. Chem. Sci.* **2018**, *1*, 31-32.
5. Castro, E.; Murillo, J.; Fernandez-Delgado, O.; Echegoyen, L., Progress in Fullerene-Based Hybrid Perovskite Solar Cells. *J. Mater. Chem. C* **2018**, *6*, 2635-2651.
6. Li, L.; Yu, Y.; Ye, G. J.; Ge, Q.; Ou, X.; Wu, H.; Feng, D.; Chen, X. H.; Zhang, Y., Black Phosphorus Field-Effect Transistors. *Nat. Nanotechnol.* **2014**, *9*, 372-377.
7. Bagheri, S.; Mansouri, N.; Aghaie, E., Phosphorene: A New Competitor for Graphene. *Int. J. Hydrogen Energy* **2016**, *41*, 4085-4095.
8. Gusmão, R.; Sofer, Z.; Pumera, M., Black Phosphorus Rediscovered: From Bulk Material to Monolayers. *Angew. Chem., Int. Ed.* **2017**, *56*, 8052-8072.
9. Zhang, R.; Li, B.; Yang, J., A First-Principles Study on Electron Donor and Acceptor Molecules Adsorbed on Phosphorene. *J. Phys. Chem. C* **2015**, *119*, 2871-2878.
10. He, Y.; Xia, F.; Shao, Z.; Zhao, J.; Jie, J., Surface Charge Transfer Doping of Monolayer Phosphorene Via Molecular Adsorption. *J. Phys. Chem. Lett.* **2015**, *6*, 4701-4710.
11. Hu, J.; Zhao, L.; Du, J.; Jiang, G., Adsorption of Rare Gases on Pristine and Doped Phosphorene. *Appl. Surf. Sci.* **2020**, *504*, 144326.
12. Gazzari, S.; Cortés-Arriagada, D., Uptake of Formaldehyde onto Doped Phosphorene Nanosheets: A Cluster Dft Study of Single and Co-Adsorption States. *J. Alloys Compd.* **2020**, *831*, 154885.
13. Zhao, Y., et al., Surface Coordination of Black Phosphorus for Robust Air and Water Stability. *Angew. Chem., Int. Ed.* **2016**, *55*, 5003-5007.
14. Yu, Z.; Song, J.; Gordin, M. L.; Yi, R.; Tang, D.; Wang, D., Phosphorus-Graphene Nanosheet Hybrids as Lithium-Ion Anode with Exceptional High-Temperature Cycling Stability. *Adv. Sci.* **2015**, *2*, 1400020.
15. Sang, D. K.; Wang, H.; Guo, Z.; Xie, N.; Zhang, H., Recent Developments in Stability and Passivation Techniques of Phosphorene toward Next-Generation Device Applications. *Adv. Funct. Mater.* **2019**, *29*, 1903419.
16. Sun, J.; Zheng, G.; Lee, H.-W.; Liu, N.; Wang, H.; Yao, H.; Yang, W.; Cui, Y., Formation of Stable Phosphorus–Carbon Bond for Enhanced Performance in Black Phosphorus Nanoparticle–Graphite Composite Battery Anodes. *Nano Lett.* **2014**, *14*, 4573-4580.
17. Rajbanshi, B.; Kar, M.; Sarkar, P.; Sarkar, P., Phosphorene Quantum Dot-Fullerene Nanocomposites for Solar Energy Conversion: An Unexplored Inorganic-Organic Nanohybrid with Novel Photovoltaic Properties. *Chem. Phys. Lett.* **2017**, *685*, 16-22.
18. Zhang, X.; Jiang, Q.; Wang, J.; Tang, J., Black Phosphorous Quantum Dots as an Effective Interlayer Modifier in Polymer Solar Cells. *Sol. Energy* **2020**, *206*, 670-676.
19. Mukhopadhyay, T. K.; Datta, A., Ordering and Dynamics for the Formation of Two-Dimensional Molecular Crystals on Black Phosphorene. *J. Phys. Chem. C* **2017**, *121*, 10210-10223.

20. Mao, J.; Ortiz, O.; Wang, J.; Malinge, A.; Badia, A.; Kéna-Cohen, S., Langmuir–Blodgett Fabrication of Large-Area Black Phosphorus-C60 Thin Films and Heterojunction Photodetectors. *Nanoscale* **2020**, *12*, 19814-19823.
21. Zhou, D.; Si, N.; Tang, Q.; Jiang, B.; Song, X.; Huang, H.; Zhou, M.; Ji, Q.; Niu, T., Defect Generation and Surface Functionalization on Epitaxial Blue Phosphorene by C60 Adsorption. *J. Phys. Chem. C* **2019**, *123*, 12947-12953.
22. Wang, C.; Niu, D.; Wang, S.; Zhao, Y.; Tan, W.; Li, L.; Huang, H.; Xie, H.; Deng, Y.; Gao, Y., Energy Level Evolution and Oxygen Exposure of Fullerene/Black Phosphorus Interface. *J. Phys. Chem. Lett.* **2018**, *9*, 5254-5261.
23. Ospina, D. A.; Duque, C. A.; Mora-Ramos, M. E.; Correa, J. D., Theoretical Study of Phosphorene Multilayers: Optical Properties and Small Organic Molecule Physisorption. *J. Mater. Sci.* **2018**, *53*, 5103-5113.
24. Perdew, J. P.; Burke, K.; Ernzerhof, M., Generalized Gradient Approximation Made Simple. *Phys. Rev. Lett.* **1996**, *77*, 3865-3868.
25. Neese, F., Software Update: The Orca Program System, Version 4.0. *WIREs Comput. Mol. Sci.* **2018**, *8*, e1327.
26. Weigend, F.; Ahlrichs, R., Balanced Basis Sets of Split Valence, Triple Zeta Valence and Quadruple Zeta Valence Quality for H to Rn: Design and Assessment of Accuracy. *Phys. Chem. Chem. Phys.* **2005**, *7*, 3297-3305.
27. Hujo, W.; Grimme, S., Performance of the Van Der Waals Density Functional Vv10 and (Hybrid)Gga Variants for Thermochemistry and Noncovalent Interactions. *J. Chem. Theory Comput.* **2011**, *7*, 3866-3871.
28. Marenich, A. V.; Cramer, C. J.; Truhlar, D. G., Universal Solvation Model Based on Solute Electron Density and on a Continuum Model of the Solvent Defined by the Bulk Dielectric Constant and Atomic Surface Tensions. *J. Phys. Chem. B* **2009**, *113*, 6378-6396.
29. Bannwarth, C.; Grimme, S., A Simplified Time-Dependent Density Functional Theory Approach for Electronic Ultraviolet and Circular Dichroism Spectra of Very Large Molecules. *Comput. Theor. Chem.* **2014**, *1040-1041*, 45-53.
30. Staroverov, V. N.; Scuseria, G. E.; Tao, J.; Perdew, J. P., Comparative Assessment of a New Nonempirical Density Functional: Molecules and Hydrogen-Bonded Complexes. *J. Chem. Phys.* **2003**, *119*, 12129-12137.
31. Boys, S. F.; Bernardi, F., The Calculation of Small Molecular Interactions by the Differences of Separate Total Energies. Some Procedures with Reduced Errors. *Mol. Phys.* **1970**, *19*, 553-566.
32. Shao, Y., et al., Advances in Molecular Quantum Chemistry Contained in the Q-Chem 4 Program Package. *Mol. Phys.* **2015**, *113*, 184-215.
33. Horn, P. R.; Mao, Y.; Head-Gordon, M., Probing Non-Covalent Interactions with a Second Generation Energy Decomposition Analysis Using Absolutely Localized Molecular Orbitals. *Phys. Chem. Chem. Phys.* **2016**, *18*, 23067-23079.
34. Horn, P. R.; Mao, Y.; Head-Gordon, M., Defining the Contributions of Permanent Electrostatics, Pauli Repulsion, and Dispersion in Density Functional Theory Calculations of Intermolecular Interaction Energies. *J. Chem. Phys.* **2016**, *144*, 114107.
35. Becke, A., *The Quantum Theory of Atoms in Molecules: From Solid State to DNA and Drug Design*; John Wiley & Sons, 2007.
36. Lefebvre, C.; Rubez, G.; Khartabil, H.; Boisson, J.-C.; Contreras-García, J.; Hénon, E., Accurately Extracting the Signature of Intermolecular Interactions Present in the Nci Plot of the

Reduced Density Gradient Versus Electron Density. *Phys. Chem. Chem. Phys.* **2017**, *19*, 17928-17936.
37. Lu, T.; Chen, F., Multiwfn: A Multifunctional Wavefunction Analyzer. *J. Comput. Chem.* **2012**, *33*, 580-592.
38. Wang, M.; Li, C. M., Magnetic Properties of All-Carbon Graphene-Fullerene Nanobuds. *Phys. Chem. Chem. Phys.* **2011**, *13*, 5945-5951.
39. Wu, X.; Zeng, X. C., Periodic Graphene Nanobuds. *Nano Lett.* **2009**, *9*, 250-256.
40. Cortes-Arriagada, D.; Sanhueza, L.; Bautista-Hernandez, A.; Salazar-Villanueva, M.; Chigo Anota, E., Chemical and Physical Viewpoints About the Bonding in Fullerene–Graphene Hybrid Materials: Interaction on Pristine and Fe-Doped Graphene. *J. Phys. Chem. C* **2019**, *123*, 24209-24219.
41. Trzaskowski, B.; Adamowicz, L.; Beck, W.; Muralidharan, K.; Deymier, P. A., Impact of Local Curvature and Structural Defects on Graphene–C60 Fullerene Fusion Reaction Barriers. *J. Phys. Chem. C* **2013**, *117*, 19664-19671.
42. Manna, A. K.; Pati, S. K., Computational Studies on Non-Covalent Interactions of Carbon and Boron Fullerenes with Graphene. *ChemPhysChem* **2013**, *14*, 1844-1852.
43. Koh, W.; Moon, H. S.; Lee, S. G.; Choi, J. I.; Jang, S. S., A First-Principles Study of Lithium Adsorption on a Graphene–Fullerene Nanohybrid System. *ChemPhysChem* **2015**, *16*, 789-795.
44. Correa, J. D.; Orellana, P. A.; Pacheco, M., Optoelectronic Properties of Van Der Waals Hybrid Structures: Fullerenes on Graphene Nanoribbons. *Nanomaterials* **2017**, *7*, 69.
45. Wu, X.; Zeng, X. C., First-Principles Study of a Carbon Nanobud. *ACS Nano* **2008**, *2*, 1459-1465.
46. Wang, G.; Slough, W. J.; Pandey, R.; Karna, S. P., Degradation of Phosphorene in Air: Understanding at Atomic Level. *2D Mater.* **2016**, *3*, 025011.
47. Pei, J.; Gai, X.; Yang, J.; Wang, X.; Yu, Z.; Choi, D.-Y.; Luther-Davies, B.; Lu, Y., Producing Air-Stable Monolayers of Phosphorene and Their Defect Engineering. *Nat. Commun.* **2016**, *7*, 10450.
48. Watts, M. C.; Picco, L.; Russell-Pavier, F. S.; Cullen, P. L.; Miller, T. S.; Bartuś, S. P.; Payton, O. D.; Skipper, N. T.; Tileli, V.; Howard, C. A., Production of Phosphorene Nanoribbons. *Nature* **2019**, *568*, 216-220.
49. Ojeda-Aristizabal, C., et al., Molecular Arrangement and Charge Transfer in C60/Graphene Heterostructures. *ACS Nano* **2017**, *11*, 4686-4693.
50. Chugh, S.; Adhikari, N.; Lee, J. H.; Berman, D.; Echegoyen, L.; Kaul, A. B., Dramatic Enhancement of Optoelectronic Properties of Electrophoretically Deposited C60–Graphene Hybrids. *ACS Appl. Mater. Interfaces* **2019**, *11*, 24349-24359.
51. Geerlings, P.; De Proft, F.; Langenaeker, W., Conceptual Density Functional Theory. *Chem. Rev.* **2003**, *103*, 1793-1874.
52. Saikia, N.; Seel, M.; Pandey, R., Stability and Electronic Properties of 2d Nanomaterials Conjugated with Pyrazinamide Chemotherapeutic: A First-Principles Cluster Study. *J. Phys. Chem. C* **2016**, *120*, 20323-20332.
53. Cortés-Arriagada, D., Phosphorene as a Template Material for Physisorption of DNA/Rna Nucleobases and Resembling of Base Pairs: A Cluster Dft Study and Comparisons with Graphene. *J. Phys. Chem. C* **2018**, *122*, 4870-4880.
54. Liu, X.; Wen, Y.; Chen, Z.; Lin, H.; Chen, R.; Cho, K.; Shan, B., Modulation of Dirac Points and Band-Gaps in Graphene Via Periodic Fullerene Adsorption. *AIP Adv.* **2013**, *3*, 052126.

55. Koh, W.; Lee, J. H.; Lee, S. G.; Choi, J. I.; Jang, S. S., Li Adsorption on a Graphene–Fullerene Nanobud System: Density Functional Theory Approach. *RSC Adv.* **2015**, *5*, 32819-32825.
56. Aijiang, L., Piezoelectric Phenomenon of Fullerene-Graphene Bonded Structure. *J. Nanomater.* **2014**, *2014*.
57. Zhou, W.-y.; Xie, S.-s.; Qian, S.-f.; Wang, G.; Qian, L.-x., Photothermal Deflection Spectra of Solid. *J. Phys.: Condens. Matter* **1996**, *8*, 5793-5800.
58. Rabenau, T.; Simon, A.; Kremer, R. K.; Sohmen, E., The Energy Gaps of Fullerene C60 and C70 Determined from the Temperature Dependent Microwave Conductivity. *Z. Phys. B: Condens. Matter* **1993**, *90*, 69-72.
59. Cortés-Arriagada, D.; Cid-Mora, F., Exploring the Adsorption Properties of Doped Phosphorene for the Uptake of DNA Nucleobases. *J. Mol. Liq.* **2021**, *325*, 115183.
60. Cortés-Arriagada, D., Intermolecular Driving Forces on the Adsorption of DNA/Rna Nucleobases to Graphene and Phosphorene: An Atomistic Perspective from Dft Calculations. *J. Mol. Liq.* **2021**, *325*, 115229.
61. Cortés-Arriagada, D.; Miranda-Rojas, S.; Cid-Mora, F.; Toro-Labbé, A., First-Principles Study of Hybrid Nanostructures Formed by Deposited Phthalocyanine/Porphyrin Metal Complexes on Phosphorene. *J. Mol. Liq.* **2021**, 115948.
62. Zheng, Y.; Xu, L.; Fan, Z.; Wei, N.; Lu, Y.; Huang, Z., Mechanical Properties of Graphene Nanobuds: A Molecular Dynamics Study. *Curr. Nanosci.* **2012**, *8*, 89-96.
63. Emami Skardi, F. S.; Ganji, M. D., Periodic Graphene Nanobuds: A Novel Li-Storage Material. *Mater. Chem. Phys.* **2013**, *142*, 44-51.
64. Liang, S.; Wu, L.; Liu, H.; Li, J.; Chen, M.; Zhang, M., Organic Molecular Passivation of Phosphorene: An Aptamer-Based Biosensing Platform. *Biosens. Bioelectron.* **2019**, *126*, 30-35.
65. Liang, H.; Xu, H.; Zhao, Y.; Zheng, J.; Zhao, H.; Li, G.; Li, C.-P., Ultrasensitive Electrochemical Sensor for Prostate Specific Antigen Detection with a Phosphorene Platform and Magnetic Covalent Organic Framework Signal Amplifier. *Biosens. Bioelectron.* **2019**, *144*, 111691.
66. Li, X.; Niu, X.; Zhao, W.; Chen, W.; Yin, C.; Men, Y.; Li, G.; Sun, W., Black Phosphorene and Pedot:Pss-Modified Electrode for Electrochemistry of Hemoglobin. *Electrochem. Commun.* **2018**, *86*, 68-71.
67. Liu, H.; Lian, P.; Zhang, Q.; Yang, Y.; Mei, Y., The Preparation of Holey Phosphorene by Electrochemical Assistance. *Electrochem. Commun.* **2019**, *98*, 124-128.